Bioinformatics, YYYY, 0–0
doi: 10.1093/bioinformatics/xxxxx
Advance Access Publication Date: DD Month YYYY
Manuscript Category

Bioimage informatics

Quantification of fibrous spatial point patterns from single-molecule localization microscopy (SMLM) data

Ruby Peters[1], Marta Benthem Muñiz[1], Juliette Griffié[1], David J. Williamson[1], George W. Ashdown[1], Christian D. Lorenz[1] and Dylan M. Owen[1*]

[1]Department of Physics and Randall Division of Cell and Molecular Biophysics.

*To whom correspondence should be addressed.

Associate Editor: XXXXXXX

Received on XXXXX; revised on XXXXX; accepted on XXXXX

Abstract

Motivation: Unlike conventional microscopy which produces pixelated images, SMLM produces data in the form of a list of localization coordinates – a spatial point pattern (SPP). Often, such SPPs are analyzed using cluster analysis algorithms to quantify molecular clustering within, for example, the plasma membrane. While SMLM cluster analysis is now well developed, techniques for analyzing fibrous structures remain poorly explored.

Results: Here, we demonstrate statistical methodology, based on Ripley's K-function to quantitatively assess fibrous structures in 2D SMLM data sets. Using simulated data, we present the underlying theory to describe fiber spatial arrangements and show how these descriptions can be quantitatively derived from pointillist data sets. We also demonstrate the techniques on experimental data acquired using the image reconstruction by integrating exchangeable single-molecule localization (IRIS) approach to SMLM, in the context of the fibrous actin meshwork at the T cell immunological synapse, whose structure has been shown to be important for T cell activation.

Availability: Analysis code available on request.

Contact: dylan.owen@kcl.ac.uk

Supplementary information: Supplementary data are available at *Bioinformatics* online.

1 Introduction

Conventional fluorescence microscopy methods produce images of an array of fluorophores within the specimen convolved with the point-spread function (PSF) of the microscope. Whilst modern fluorescence microscopes are capable of detecting photons originating from a single fluorophore, the diffraction limit of light impedes the ability of these instruments to spatially resolve such information, thereby imposing an image resolution of approximately 200 nm under ideal conditions. Recently, several key technologies capable of circumventing the 'diffraction barrier' have been developed; 'super resolution' microscopy. In particular, single-molecule localization microscopy (SMLM) methods are capable of approximately 10 - 30 nm lateral resolution, achieved through the temporal separation of individual PSFs thereby preventing multiple PSF overlap at the detector, which would otherwise degrade image quality (Betzig, et al., 2006; Hess, et al., 2006; Rust, et al., 2006). SMLM techniques are highly dependent upon physiochemical properties (Dempsey, et al., 2011; Heilemann, et al., 2008) of fluorescent dyes and powerful localization algorithms (Sage, et al., 2015). Unlike conventional microscopy methods,

which produce raster images with pixel values representative of local fluorescence intensity, SMLM images comprise of a list of Cartesian molecular coordinates of all localized emitters, each with an associated estimated uncertainty (Thompson, et al., 2002). The analysis of spatial point patterns (SPPs) therefore necessitates a different statistical approach to conventional microscopy.

Several strategies for SPP analysis exist and have been well tested for examining molecular clustering across diverse biological systems. Common statistical methods of 2D SPP analysis rely upon correlation functions to identify clustered, dispersed or random distribution patterns. A widely used correlation-based analysis is the pair correlation function (PCF) (Sengupta, et al., 2011), which computes the probability that the location of one event is within a distance r of another event. Another method of SPP analysis is based upon Ripley's K-function (Owen, et al., 2010; Ripley, 1977). The K-function function is closely related to the PCF, in the sense that both methods measure spatial association of events, within cumulative circles (K-function) or tori (PCF). This method (K-function analysis) predates super resolution microscopy, having been previously used in electron micrograph studies of proteins in the plasma membrane (Prior, et al., 2003) and more recently to describe surface protein heterogeneity in SMLM data sets (Owen, et al., 2010). The unique feature Ripley's K-function is its ability to characterize the dominance of spatial point processes over a wide range of distances; information that often pertains to cellular response. Mathematically, the K-function is estimated as:

$$K(r) = \frac{A}{n^2} \sum_{i=1}^{n} \sum_{j=1, i \neq j}^{n} \frac{\delta_{ij}}{w_{ij}}$$

Where δ_{ij} is unity if the point-to-point distance of the i^{th} and j^{th} events is less than r, and n is the number of events in area A, for $i \neq j$. The weighting term w_{ij} accounts for edge effects. For a completely spatially random (CSR) distributed SPPs, $\langle K(r) \rangle = \pi r^2$ for all r. Linearization of the K-function, $L(r) = \sqrt{(K(r)/\pi)}$, is often easier to interpret, since under CSR, L(r)=r and its variance remains constant. Normalization of the K-function results in the H-function, H(r)=L(r)-r, often used to determine deviations from the expectation value $\langle H(r) \rangle$ evaluated at each r to test for randomness. For a SPP consisting of clusters, H(r) exhibits a maximum at a characteristic r, correlated to the cluster size. Descriptors of molecular clustering are commonly extracted using K-function analysis, however quantification of fibrous structures, rather than clusters, in SPPs generated by SMLM remains unstudied.

A requirement of all SMLM techniques is achieving a high enough labelling density for high-fidelity image reconstruction and detection of events, in unison with high localization precision. A recently developed SMLM method, IRIS (Kiuchi, et al., 2015), has demonstrated unparalleled labelling density across various cellular structures, thereby offering a considerable improvement to conventional probe methods. IRIS probes are small fluorescently labelled protein fragments which rapidly bind and unbind to their specific target structures. Transiently bound probe can be imaged in total internal refection mode (TIRF) and integrated over many frames to form a pointillist map of localizations. Using the IRIS approach to SMLM, we are able to observe the distribution of filamentous (F-) actin at the T cell immunological synapse. This dense actin network forms directly beneath the plasma membrane (Babich, et al., 2012; Burkhardt, et al., 2008) and has been shown to be crucial for multifarious cellular processes. Specifically, it has been demonstrated that actin plays an important role in T cell activation; vital when mounting an immune response. Immunological synapse formation is typically initiated though the coupling of peptide-bound major histocompatibility complexes (pMHC) on the surface of antigen presenting cells (APC), with the cognate T cell receptor (TCR). Triggering of the TCR initiates a cascade of signaling effectors which drive extensive remodeling of the actin cytoskeleton (Beemiller and Krummel, 2010). Understanding the nanoscale architecture of this network, in a quantitative manner, is vital to furthering our understanding of the T cell activation process.

Here, we present statistical methodology based upon Ripley's K-function to identify key descriptors of fibrous SPPs. We demonstrate, using a variety simulated SPPs, that we can accurately evaluate inter-fiber spacing through K-function analysis. We present a novel modification of Ripley's K-function which considers the relative density of points within a specific angular range. Ripley's K-function analysis based on angular dispersion, termed K(α), provides a method of determining fiber characteristics. We then use this technique to analyze the fibrous distribution of F-actin at the T cell immunological synapse: the distribution of which is of great interest and importance for T cell activation.

2 Methods

2.1 Cell culture

Jurkat E6.1 T cells (ATCC TIB-152) were cultured in Roswell Park Memorial Institute (RPMI-1640) medium supplemented with 10% fetal bovine serum (FBS) and 1% Penicillin/Streptomycin. To create T cell synapses, 8-well chamber slides were coated with anti-CD3 (clone OKT3) and anti-CD28 (clone 28.2) antibodies (Cambridge Bioscience and BD Bioscience, UK) in phosphate buffered saline (PBS) at a concentration of 2 µg/mL and 5 µg/mL respectively and left overnight at 4°C.

2.2 IRIS and dSTORM imaging

Prior to imaging, stimulatory (anti-CD3/anti-CD28 coated) coverslips were gently washed with PBS to remove surplus antibody in suspension. Coverslips were temperature equilibrated prior to plating the cells. Cells were seeded at 3×10^5 cells/mL and re-suspended in pre-warmed RPMI supplemented with 10% FBS. Cells were placed on the stimulatory coverslip for 2 or 10 minutes at 37°C to allow synapse formation (Williamson, et al., 2011). Surplus medium was then removed and the attached cells were quickly fixed with pre-warmed cytoskeletal buffer (CB; 10 mM MES (6.1 pH), 5 mM EGTA, 5 mM fresh glucose, 150 mM NaCl pH. 7.0) containing 4% paraformaldehyde (PFA) for 15 minutes at 37°C. Post fixation, synapses were washed with CB several times and cells permeabilized with 0.1% Triton-X-100 for 5 minutes at 4°C. The sample was washed 6 times with PBS and blocked with Image iT-FX signal enhancer (ThermoFisher) for 30 minutes at room temperature. The blocking agent was removed and the LifeAct-Atto655N IRIS (Kiuchi, et al., 2015) probe added at 0.5 nM in PBS. For dSTORM, cells were fixed, permeabilised, washed 6 times with PBS and labelled with phalloidin conjugated AlexaFluor 647 (Thermo Fisher, USA) at a final concentration of 165 nM overnight at 4°C. The sample was washed in PBS 6 times and imaged in an oxygen-scavenging buffer system consisting of: 20 µg/ml catalase, 10% glucose, 4 % Tris (2-carboxyethyl) phosphine hydrochloride, 50 % glycerol, 25 mM potassium chloride, 20 mM pH 7.5 Tris and 1mg/ml glucose oxidase in diH20, and 1 M Cysteamine-HydroChloride.

2.3 Microscope settings

A commercial N-STORM system (Nikon, Japan) was used in TIRF mode to perform all IRIS imaging, with a 100×1.49 NA oil-immersion objective lens. After selecting an appropriate region of interest (ROI) (512×512 pixels), the 647 nm laser was applied at 50% power (approximately 1.125 kW/cm^2), to limit signal acquired from freely diffusive unbound probe. Images were acquired at 50 ms integration time for 100,000 frames. For dSTORM, 50,000 frames were acquired with an integration time of 20 ms and imaged using 100% laser power.

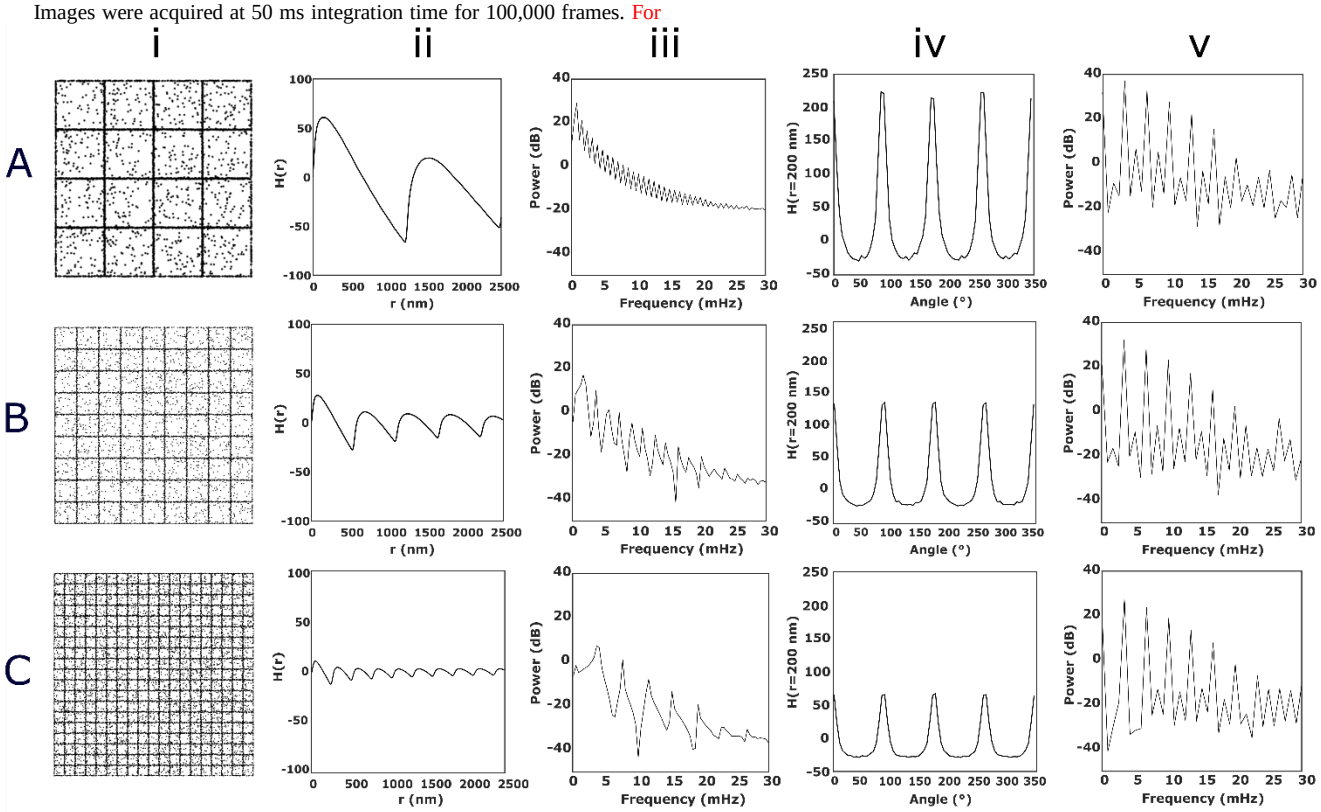

Fig. 1: Ripley's H(r) and H(α) analysis of regular, perpendicular FSPPs of varying inter-fiber spacing's. Simulations of 1250 nm (A), 555 nm (B) and 260 nm (C) inter-fiber spacing's were generated with points added to each fiber every 15 nm with up to 15 nm localization uncertainty. The entire FSPP was then subject to background containing 30% of the number of localizations assigned to fibers. Ripley's H(r) curves were computed (ii) and their corresponding power spectra (iii). Ripley's H(α) curves (iv) and their spectra (v) are also presented for the three simulations.

2.4 Image reconstruction

All image reconstruction and post-processing was performed using the ImageJ plug-in ThunderSTORM (Ovesný, et al., 2014). Images were filtered using a 3rd order B-spline wavelet filter. Single molecule localizations were estimated using a local maximum method with 8-neighbourhood connectivity. The PSF method of sub-pixel localization was used with a least-square fitting approach. Post processing consisted of drift correction via cross correlation and uncertainty filtering retaining localizations less than 15 nm, as calculated by the method of Thompson et al (Thompson, et al., 2002). Localizations that appeared in more than 20 consecutive frames within a radius of 20 nm were merged.

3 Results

3.1 Regular perpendicular fibrous patterns

We begin by defining the classification of a square ROI (5 x 5 μm) containing fibrous spatial point patterns (FSPPs) into three distinct classes: Regular, Random and Bundled. First, we consider the case of a Regular FSPP, consisting of an equal number of horizontal and vertical fibers arranged orthogonal to one another and to the axis of intersection (Fig. 1). Here, we simulated Regular FSPPs with various inter-fiber spacing's. Points were placed at regular intervals, every 15 nm, along each fiber. All point positions were then scrambled by up to 15 nm to simulate localization uncertainty. The whole pattern was then overlaid with a CSR distribution of non-fibrous points accounting for 30% of the total number of fibrous points. The inter-fiber spacing of a Regular FSPP is consistent along both x and y axes, and can be recovered through Ripley's H(r) analysis (Fig. 1) despite localization uncertainty and noise. The FSPPs for an inter-fiber spacing of 1250 nm (Fig. 1A), 555 nm (Fig. 1B) and 260 nm (Fig. 1C) are shown in Fig. 1i. The resulting Ripley's H-function curves (Fig. 1ii) demonstrate a clear periodic pattern, with minima reflective of the simulated inter-fiber spacing. The power spectral density of a physical process, in this case defined by H(r), encompasses fundamental information pertaining to the nature of the H-function. Computing the power spectral density spectrum transforms H(r) into the frequency domain (Fig. 1iii). In this case, the regular position of peaks within the frequency spectrum is reflective of the periodic nature of H-function. Therefore, the time period of the power spectral density function is inherently related to the occurrence of fibers within the SPP: the inter-fiber spacing. In this case

(Fig. 1A), the separation of peaks in the power spectrum is 0.8 mHz corresponding to a period in the H-function of 1250 nm, i.e. the specific simulated inter-fiber spacing.

By using a variant of Ripley's H(r)-function based upon angular dispersion, termed H(α), one can ascertain the nature of an SPP. This involves computing the K (r = 200 nm) function within a specific angular range (in this case 5° intervals) starting from a reference vector aligned with the y-axis for each point in the SPP. H(α) is defined in a similar way to H(r), but incorporating a correction term to account for the differing area in which points are counted such that the K-function is calculated using:

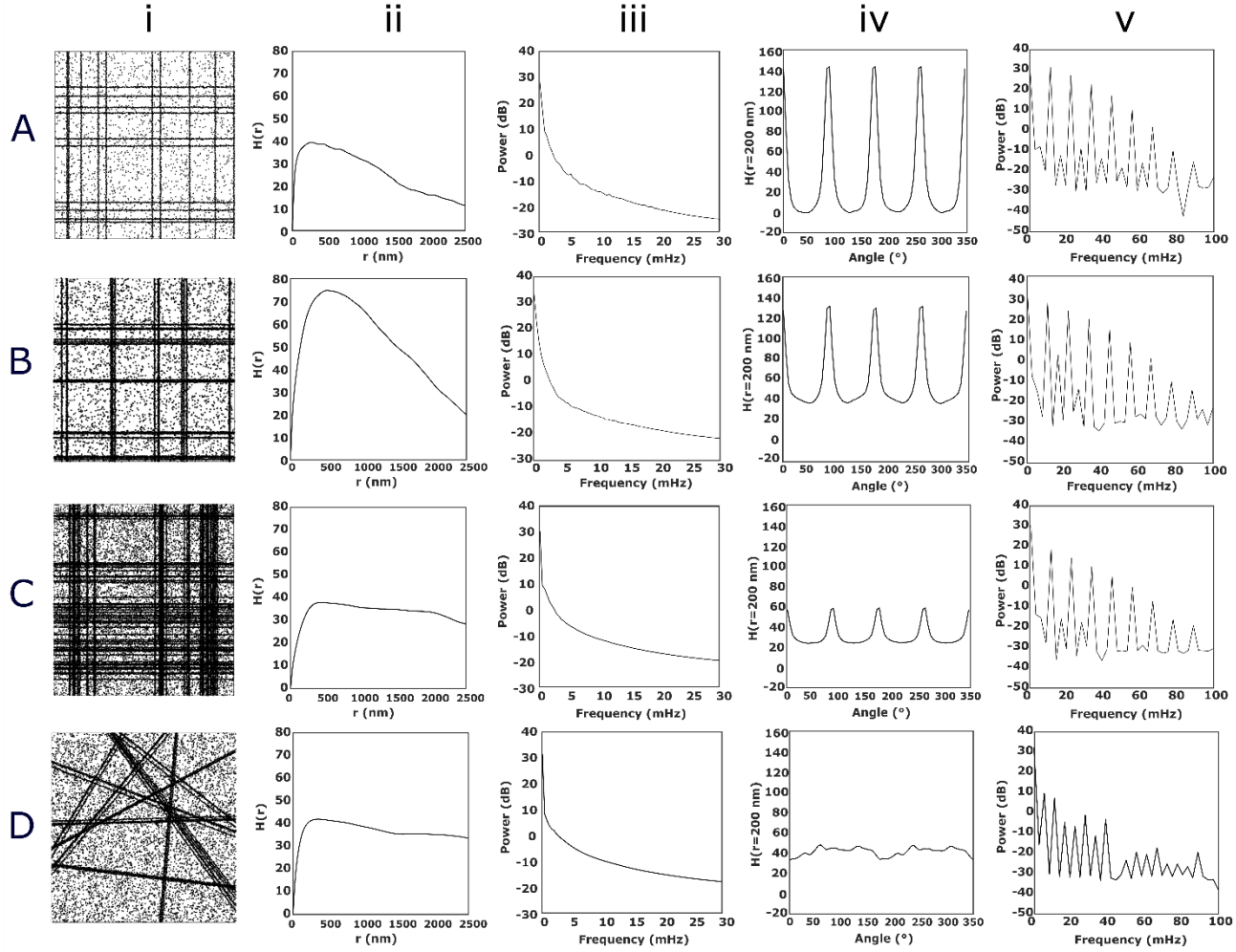

Fig. 2: Ripley's H(r) and H(α) analysis of random fibrous spatial point patterns of varying bundling properties. A representative example (from n=50 simulations) of 10 randomly placed fibers per axis (A). Representative examples (from n=50 simulations) of bundled fibrous distributions, (B) and (C), simulated with 5 bundles per axis with 3 fibers per bundle in (B) and 10 per axis with 5 fibers per bundle in (C). A representative example (n=50 simulations) of 10 bundled fibrous distributions with 3 fibers per bundle generated at random angles across the ROI (D). All fibers were generated with points added to each fiber every 15 nm with up to 15 nm localization uncertainty. The entire FSPP was then subject to 30% non-fibrous background. Averaged Ripley's H(r) curves were computed (ii) and their corresponding power spectra (iii). Averaged Ripley's H(α) curves (iv) and their spectra (v) are also presented for the three FSPP classes.

$$K(\alpha) = \frac{360}{5}\frac{A}{n^2}\sum_{i=1}^{n}\sum_{j=1,i\neq j}^{n}\frac{\delta_{ij}}{w_{ij}}$$

The mean H(α) value for all points in the SPP is then calculated for each value of α: For regularly spaced, perpendicular fibers, one would expect that H(α) exhibit maxima at 90° intervals from the normal reference vector. This result is indicative of perpendicular fibrous structures (Fig. 1iv). In this case, a peak is observed every 90° as expected, regardless of inter-fiber spacing. As with the H(r)-function, we are able to compute the power spectral density function for H(α) (Fig. 1v). Again, peak spacing in this spectrum corresponds to periodicity in the H(α) function. In Fig. 1A for example, peak spacing is 11.1 mHz, corresponding to a periodicity of 90°. To test the effect of varying the fixed radius (here 200 nm), we repeated

the analysis for the Standard Condition data set (Figure 1A) for a range of radii, from 0 to 2500 nm. Supplementary Figure 1 demonstrates that the calculated values of H(α) are largely insensitive to this choice of parameter up to ~750 nm where the diagonals across the fibrous mesh are detected at intervals of 45°. Further, we tested the effect of increasing the percentage of non-fibrous background localisations on the analysis (Supplementary Figure 2). For each condition (A = 30%, B=60%, C=90% of localisations in the background), the peak spacing in the power spectrum corresponds to the simulated inter-fiber spacing demonstrating that the analysis is robust even when up to 90% of points are in the non-fibrous background. Finally, to better represent experimental data, we simulated fibers in which the labelling efficiency is uneven such that there is a varying density of points along the fibers. Supplementary Figure 3 shows analysis of Standard Condition data sets in which the labelling efficiency is 100% of that in Figure 1A (Supplementary Figure 3A), reduced by 50% (Supplementary Figure 3B) and reduced by 75% (Supplementary Figure 3C). The analysis is robust to these conditions.

3.2 Random perpendicular FSPPs

In the next case, we examine randomly arranged perpendicular fibers. These have their axis intersection positions defined by a 1D CSR distribution. An example of such an arrangement (from a total of n = 50 simulations) is shown in Fig. 2A. The resulting mean H(r)-function from all 50 simulations is displayed (Fig. 2Aii), and its associated power-spectral density function (Fig. 2Aiii). In this case no periodicity is observed in the H(r)-function, as expected for such a random arrangement. Therefore, the conventional H-function and its power spectrum provides a way to distinguish between regular and random perpendicular fibers. As in the regular case, the angular H-function, H(α), (Fig. 2Aiv) and its power spectrum (Fig. 2Av) demonstrate that the fibers are perpendicular to one another and to the axis of intersection.

3.3 Random bundled FSPPs

The final interesting case for linear, perpendicular fibers is a FSPP in which fibers form bundles (Fig. 2B-C). To form our Bundled FSPP, we define the number of bundles (5 per axis in Fig. 2B and 10 per axis in 2C) and the number of fibers assigned to each bundle. The bundling behaviour of actin has been shown to be important for a range of cellular processes (Bathe, et al., 2008; Claessens, et al., 2006; Gowrishankar, et al., 2012). Therefore, quantitative knowledge on the bundling behavior of fibers could be of great interest. We begin by generating random positions for the centers of each bundle on each axis. For the individual fibers (3 per bundle in the case of Fig. 2B, and 5 in the case of Fig. 2C), we draw a random number that determines the fiber position from a normal distribution with mean parameter μ (the center of the bundle) and standard deviation σ (the bundle width, 100 nm in this case). For the case of low bundling (Fig. 2B), the H(r)-function height is increased with respect to unbundled fibers,

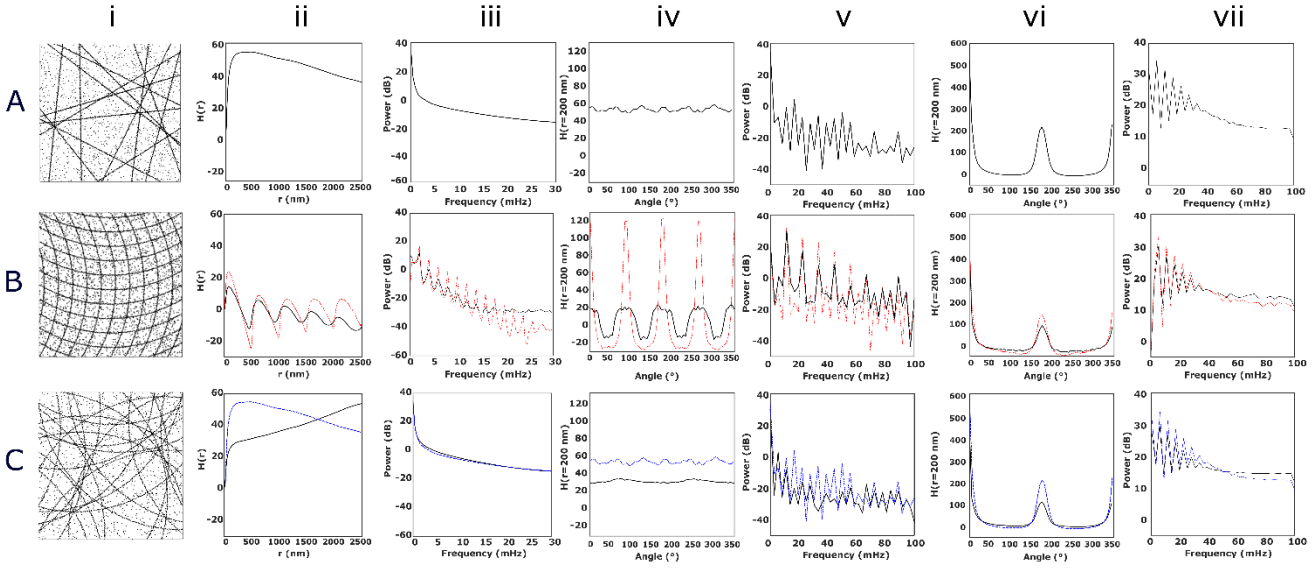

Fig. 3: Ripley's H(r) and H(α) analysis of FSPPs of varying fiber architectures. A representative example (from n = 50 simulations) of 15 randomly placed linear fibers across the ROI, (A). A regular curved (radius of curvature = 5000 nm) perpendicular FSPP is presented in (B) and an example (from n = 50 simulations) of a random, non-perpendicular FSPP with the same radius of curvature is presented (C). All fibers were generated with points added to each fiber every 15 nm with up to 15 nm localization uncertainty. The entire FSPPs were then subject to background containing 30% of the number of localizations assigned to fibers. Ripley's H(r) curves were computed (ii) and their corresponding power spectra (iii). Ripley's H(α) curves (iv) and their spectra (v) and the shift corrected analogues (vi) and (vii) are also presented for the three representative FSPPs classes. The results for a regular, linear, perpendicular FSPP of the same simulation conditions as (Bi) is also shown (red dashed line) for direct comparison. In addition, both results for the random FSPPs with curvature (C) (black lines) and the random linear FSPPs shown in (A) are presented (blue dashed lines) for clear comparison.

indicative of increased clustering of points. As the bundle density increases, the height of H(r) decreases and its width increases as the ROI becomes increasingly fiber abundant. The angular H-function (Fig. 2iv) and its power spectrum (Fig. 2v) continue to show perpendicular fibers. Simulations of non-perpendicular fibrous bundles were performed and analyzed using H(r) and H(α) (Fig. 2D). In this case, the lack of perpendicularity of the fibrous structures was evidenced by the H(α) curve (Fig. 2D

iv). Further, we tested the analysis with simulated data of increasing bundling widths (Supplementary Figure 4A-C) and differing bundling widths within the same ROI (Supplementary Figure 4D). The H(r) analysis demonstrated a broadening and a shift to higher radii as the bundle width increased. The H(α) analysis accurately identified the presence of perpendicular fibrous structures.

In the case of almost any biological system, FSPPs do not consistently display perpendicular fiber architecture. Hence, we next simulated non-perpendicular FSPPs (Fig. 3A), wherein fibers are placed at random across the ROI. This condition is achieved through generating two uniformly distributed random coordinates within the ROI, for each fiber. A fiber is placed to intersect both points and extrapolated across the ROI. An example (from n = 50 simulations) of such a distribution is shown in in Fig. 3Ai. As expected, the mean H(r)-function (Fig. 3Aii) and its power spectrum (Fig. 3Aiii), do not show any periodic behavior. Importantly, the H(α) curve (Fig. 3Aiv) and its power spectrum (Fig. 3Av), do not show periodic behavior demonstrating that these fibers are not orthogonally arranged. H(α) is therefore a useful tool to discriminate between perpendicular and non-perpendicular fiber arrangements. For heterogeneous fiber orientations such as this, it is possible to further modify the H(α) function to generate additional information. The H(α)-function for each point in the FSPP can be shifted such that its maxima lies at α = 0˚, before averaging the curves from each event. This becomes necessary as the H(r)-function has an intrinsic start at r = 0 nm whereas H(α) has α = 0° at an arbitrary vector position in the FSPP (along the y axis). In this way, we are able to demonstrate the presence of a fibrous pattern, even for randomly arranged fibers, as they will display a prominent peak in the shift corrected H(α)-function at α=180°. In this case, the shifted H(α)-function (Fig. 3Avi) and its power spectrum (Fig. 3Avii), do indeed display periodicity with a period of 180°.

In terms of biological context, the next level of complexity involved generating non-linear FSPPs. We began by simulating a regularly spaced curved FSPP, by generating horizontal and vertical counter-clockwise circular arcs at equally spaced intervals along both the x and y axis, across the ROI (Fig. 3B). The radius of curvature was globally set to 5000 nm. An example of such a simulation is shown (Fig. 3Bi). Ripley's H(r)-function (Fig.3Bii) and its power spectrum (Fig. 3Biii) demonstrates that the inter-fiber spacing for the curved FSPP can be accurately determined in the presence of localization uncertainty, in the same way as for linear fibers. In this case, the spacing was set to 500 nm, and this is recovered from H(r) and its spectrum. By examining the H(α) curve (Fig. 3Biv) and its spectrum (Fig. 3Bv), the presence of regular fibers is observed. Interestingly, in comparison to linear fibers (red dashed lines), the height (defined as the distance from the curve minimum to its maximum) of the H(α) peaks are decreased from 162.40 ± 0.31 to 64.46 ± 0.33 nm (S.E.M, n=50, p<0.0001) indicating the presence of high-density points at a greater range of angular positions; the hallmark of curvature. This behavior is also reflected in the angular shift corrected H(α) curve analysis (Figs. 3B vi and vii) in which the height of the central peak is decreased from 200.80 ± 0.40 to 187.40 ± 0.57 nm (S.E.M, n=50, p<0.0001).

Finally, we generate FSPPs consisting of 25 randomly placed fibers of known curvature (R = 5000nm). We define randomly placed fibers by generating two randomly selected arc intersection coordinates within the ROI for each fiber, and randomly choosing either a counter-clockwise or clockwise circular arc. An example of such an FSPP is shown (Fig. 3Ci) (representative from n = 50 simulations). Similar to the case of randomly placed, non-perpendicular linear fibers (Fig. 3A), no periodic behavior is observed in the H(r) curve (Fig. 3Cii) or its power spectrum (Fig. 3Ciii),

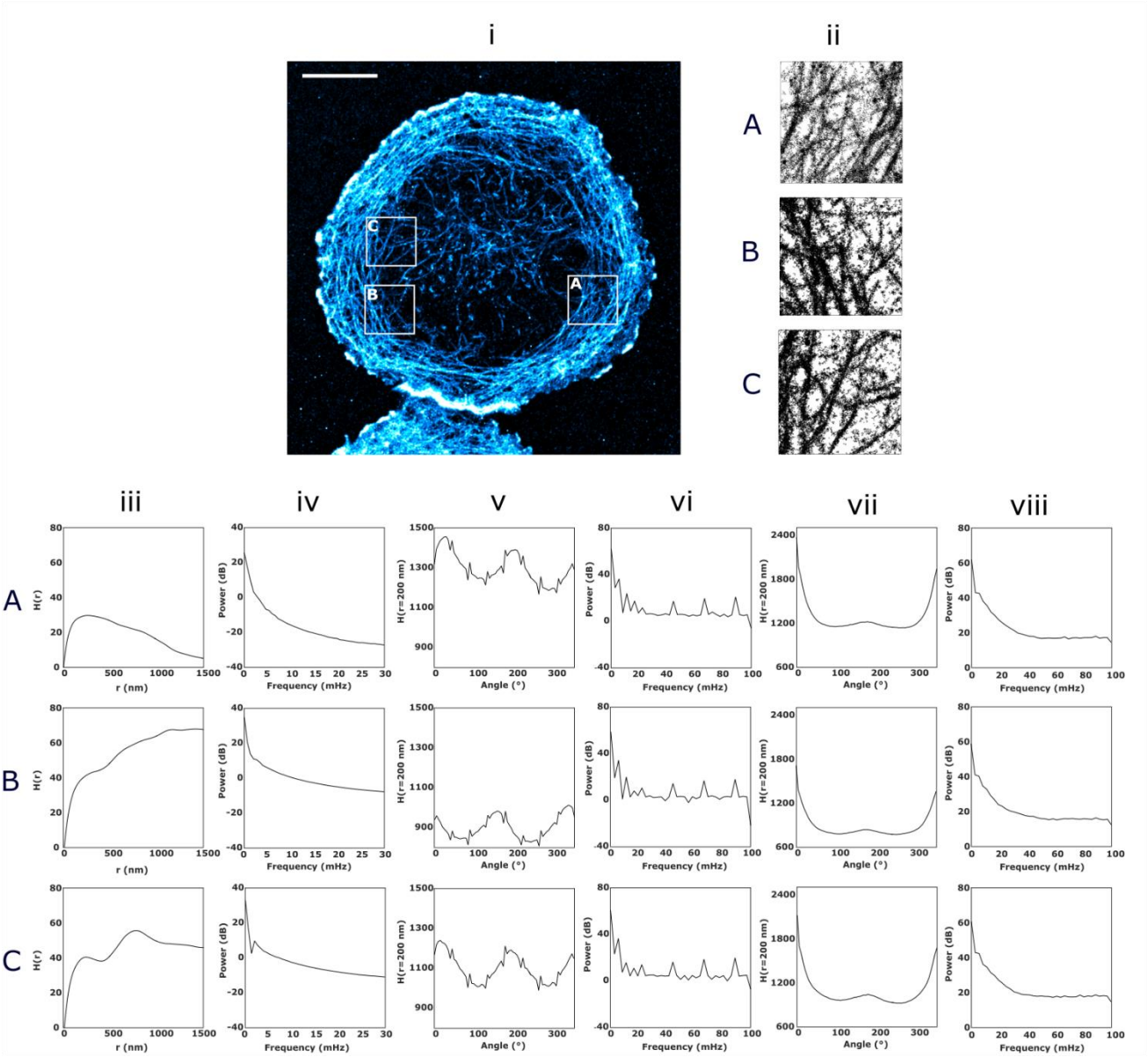

Fig. 4: Application of Ripley's H(r) and H(α) functions to experimental data using the IRIS technique. Jurkat T cell synapses (10-minute activation) were engineered on stimulatory coverslips (see Methods) and imaged using the IRIS approach to SMLM. A representative IRIS image of the F-actin distribution at the mature T cell synapse is shown in (i), from which three (3×3 μm) ROIs of the synapse periphery were selected (A-C ii). Conventional H(r) analysis was performed (iii) and power spectra generated (iv). Ripley's H(α) curves (iv) and their power spectra (v) and the shift corrected analogues (vi) and (vii) are also displayed.

as expected. Likewise, H(α) (Fig. 3Civ) and its spectrum (Fig. 3Cv) do not demonstrate the presence of perpendicular fibers, but the shift corrected curves (Fig. 3Cvi and vii) display a peak at 180° of height (64.46 ± 0.33 nm which is less prominent than the linear fiber case (blue dashed lines, 112.30 ± 0.99 nm, S.E.M, n=50, $p<0.0001$), indicative of curvature.

Using simulated data, we have demonstrated that H(r) and H(α) are capable of discerning perpendicularity and curvature in structures generated from FSPPs. We next apply our methodology to experimental biological data. As an example, we have chosen to analyze the cortical actin meshwork at the T cell immunological synapse (Bromley, et al., 2001). Data was acquired using the IRIS (Kiuchi, et al., 2015) approach to SMLM producing FSPPs of the distribution of F-actin. A representative example of an IRIS image of F-actin at the T cell synapse is shown in Fig. 4i, from which three regions were selected for analysis (Fig. 4ii). The H(r) curves (Fig. 4iii), their power spectra (Fig. 4iv), the non-shifted H(α) curves (Fig. 4v) and their spectra (Fig. 4vi) and finally the shift corrected H(α) curves (Fig. 4vii) and their spectra (Fig. 4viii) are displayed. The H(r) spectra show that there is no periodicity in the H-function, unlike a regular, perpendicular FSPP, indicating a non-regular arrangement of actin at the T cell synapse. Examining the non-shifted H(α) curves and their spectra reveals that whilst the fibers are not perpendicular, they are also not ran-

domly orientated. This is evidenced by the periodicity in H(α) with characteristic peak separation of 180°, which is also evidence of a fibrous rather than a clustered distribution. In contrast to the perpendicular fibers

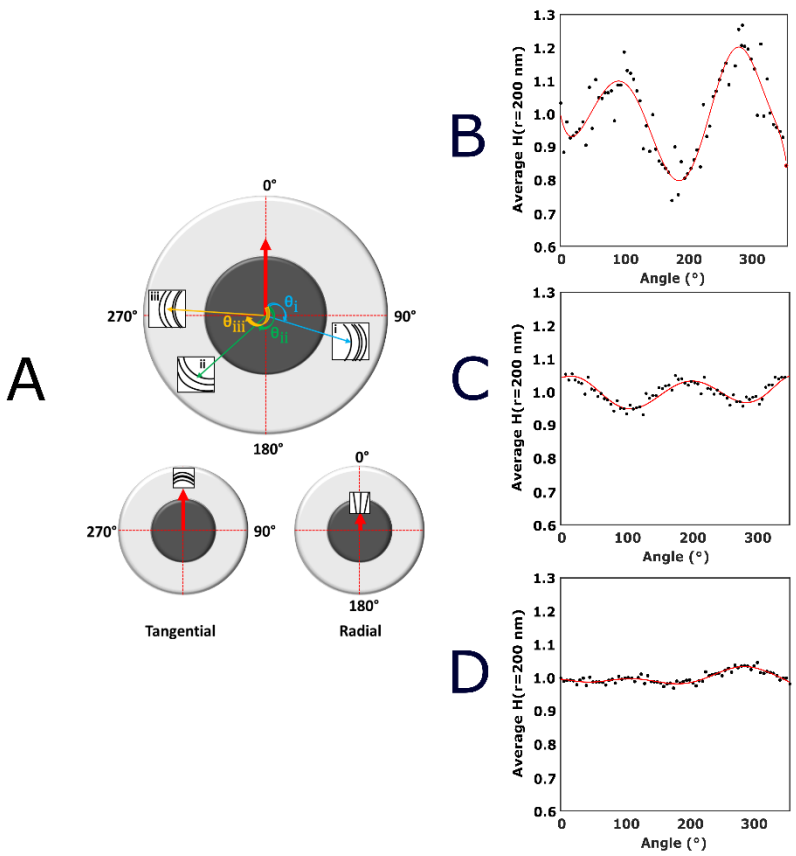

Fig.5: Post-processing of H(α) reveals fiber orientation across multiple ROIs. Schematic representation (A) of the mature (10 minute) T cell synapse constituting the central region (depicted dark grey) and the cell periphery (depicted light grey) in which F-actin forms concentric ring-like structures. Correcting the H(α) curves for each region (i, ii, iii) by their corresponding angular displacement (Θi, Θii and Θiii) from the y axis reference (depicted solid red) enables a clear description of global fiber orientation; the two extremes of which are radial and tangential, with respect to the reference vector. For the 10-minute T cell synapse (Fig. 4), a summation of post-processed H(α) curves for the cell peripheral regions is presented (B), normalised by their average H(α), from the three ROIs depicted in (Fig. 4A-C). A summation of post-processed H(α) curves for the cell central regions (Supp. Fig 5) is also presented (C). For the 2-minute T cell synapse (Supp. Fig. 7), a summation of post processed curves, normalised by their average H(α), is presented (D) from the three ROIs (Supp. Fig 7). All post-processed curves are overlaid with an 8th order fitting polynomial.

considered earlier, the non-shifted H(α) curves exhibit two prominent peaks rather than four, an indication that the majority of fibers are orientated in a similar direction. In the case of Fig. 4A for example, at approximately 20° relative to the y-axis. Examination of the shifted H(α) curves and their spectra demonstrate a characteristic central peak at 180° which is low (77.66 ± 8.22 nm, S.E.M, n = 3), earlier demonstrated to be evidence for curvature. In these examples, the most extreme case of curvature is found in Fig. 4C. To test the sensitivity of the method, we repeated the analysis for 3 regions in the synapse center (Supplementary Figure 5). Analysis of the shifted H (α) curved demonstrate a decrease in height from 77.66 ± 8.22 nm in the peripheral regions to 38.55 ± 11.07 nm in central regions (S.E.M, n=3, p = 0.047). This indicates a subtle change in fiber architecture in which fibers display increased curvature in peripheral regions. To validate the necessity of using IRIS, we also acquired data using dSTORM via phalloidin coupled to Alexa-647 (Supplementary Figure 6). The data confirms that acquired by IRIS i.e. the presence of non-perpendicular fibrous structures. However, in agreement with our simulated data (Supplementary Figure 3) while the analysis remains robust to the lower labelling density generated by dSTORM, signal-to-noise is degraded making the description of the structure more challenging.

Further post-processing of the non-shifted H(α) values provides additional information regarding fiber orientation with respect to the entire T cell. A cell reference vector can be defined between the cell center and the ROI center (Fig. 5A). The H(α) analysis can then further discriminate between tangential and radial fibrous structures. We began by computing the angle between the cell reference vector and the y axis, termed θ_i, for the i^{th} ROI. These θ_i values were then used to translate the corresponding H(α) values to compensate for angular disparities in the position of ROIs within the cell periphery. Using this method, we can assess the dominance of fiber orientation, at different time-points of synapse maturation. Early synapses (2 mins post-activation) were analyzed using conventional H(r) and H(α) (Supplementary Figure 7) and compared to 10 minute synapses using the post-processing method (Fig. 5). The resultant H(α) curves from each of

three ROIs per condition could then be summed and normalized to assess the dominance of fiber alignments within the cell, with respect to the cell reference vector. This enables the direct comparison of fibrous structures observed within different ROIs between conditions.

In terms of our biological system, for mature synapses we expected that the majority of fibrous structures would be observed at angles orthogonal to the cell reference vector, since F-actin forms a series of concentric fibers around the cell periphery at this synapse maturation stage (Babich, et al., 2012; Burkhardt, et al., 2008). For the three ROIs (Fig. 4A-C), the dominance of tangential fibers at the cell periphery was evidenced by the two prominent peaks in the post-processed H(α) curve (Fig. 5B) at 90° and 270° with modulation depth 0.98 ± 0.25 nm (S.E.M, n = 3). Interestingly, no peaks were observed at 0° and 180°, therefore suggesting that there was not a subpopulation of radial fibers within the three given ROIs. When we select and analyze central regions (Supplementary Figure 5) however, we detect a difference in fibre orientation with respect to peripheral regions, as evidenced by peaks in the post-processed H(α) curves at 0° and 180° (Fig. 5C, modulation depth 0.17 ± 0.03 nm, S.E.M, n = 3). In early stage synapse (2-minute post-activation) formation (Fig. 5D), the modulation depth is significantly decreased to 0.10 ± 0.01 ($p = 0.0307$ relative to peripheral regions in the 10 min case). This indicates that there is a lower dominance of tangential fibers at this time-point. While it is in principle possible to analyze a whole cell as a ROI, due to very heterogeneous fiber architectures, subtle variations between regions will be averaged out.

In this work, we present the use of Ripley's K-function and a novel variation thereof, for the analysis of pointillist patterns with fibrous structures, such as those generated by SMLM. SMLM achieves an image resolution in the range 10 – 30 nm, an order of magnitude higher than conventional resolution microscopy. This permits the study of fine fibrous structures whose inter-fiber spacing is otherwise unresolvable and therefore unquantifiable.

Using simulated data of various FSPP architectures we are able to discriminate between perpendicular, non-perpendicular and randomly orientated fibers. In the case of perpendicular, regularly spaced fibers, the method is able to accurately determine the inter-fiber spacing despite the presence of localization uncertainty and background signal originating from non-fiber associated points. In addition, our method is able to discern between regular, random and bundled fiber distributions. Introducing fiber curvature, we demonstrate that the method can discriminate between linear and curved FSPPs, in addition to perpendicularity.

We tested our approach using data generated by IRIS imaging of F-actin, whose distribution has been shown to be important for the regulation of membrane protein diffusion and clustering via the so-called Picket Fence Model (Kusumi, et al., 2005; Murase, et al., 2004). By exploiting the IRIS technique, not only are we are routinely able to achieve a lateral resolution of approximately 10 nm, we are also able to achieve extremely high labelling density of target structures, thereby revealing the nanoscale architecture of fine F-actin. In this case, we demonstrated our method by quantifying F-actin architecture at the T cell immunological synapse.

Previous studies have attempted to analyse fibrous structures arising from SMLM techniques. These have included the use of polarisation-resolved imaging to extract the direction of fluorophore dipoles (Valades Cruz, et al., 2016) and the use of Ripley's cross-correlation and Fourier transforms to detect co-orientation between fibers detected in separate colour-channels (Nieuwenhuizen, et al., 2015). The method presented here is the first to extract global information from spatial-point patterns including mesh spacing, curvature and fiber co-orientation. Here, we analyzed actin structures at T cell synapses using the IRIS approach to SMLM (Kiuchi, et al., 2015). This has the advantage over more traditional PALM/dSTORM (Betzig, et al., 2006; Heilemann, et al., 2008) that the number of available fluorophores is very high, allowing dense labelling of the underlying structures. Further, the small size of the probe and the ability to select only those localizations with high theoretically-calculated localization precisions maximizes image resolution. IRIS also does not require the overexpression of actin which can affect cell morphology and behaviour. Like all SMLM methods, IRIS may be subject to the problem of multiple-blinking of fluorophores such as that reported for dSTORM and PALM methods (Annibale, et al., 2010; van de Linde, et al., 2010). While there are a number of palliative approaches to this problem (Annibale, et al., 2011; Annibale, et al., 2011; Baumgart, et al., 2016), these are not necessary here, since the absolute number of localizations is not a required output for the analysis.

Our results indicate that cortical actin at the peripheral region of the synapse is curved but possesses co-linearity, showing an organized architecture in which the fibers are not randomly arranged. We have demonstrated that further post-processing of H(α) enables a quantitative description of fiber orientation across multiple ROIs. Correcting for ROI angular disparity with respect to the center of the immune synapse provides a clear discrimination between tangential and radial fibrous structures. Our analysis indicates that peripheral regions of the immunological synapse present a clear abundance of tangential fibrous structures.

The H(α) analysis provides additional information to conventional H(r) for detecting curvature, periodicity and fiber orientation. This makes it an important advance for the study of fibrous point patterns generated by SMLM. In conclusion, while statistical analysis of fibrous SPPs produced by SMLM techniques remains unstudied, relative to their clustered counterparts, we have demonstrated here that existing techniques can be modified to extract quantitative descriptions of FSPPs.

Acknowledgements

We acknowledge Helge Ewers for providing the IRIS probe. Imaging was performed in the Nikon Imaging Centre, King's College London.

Funding

This work has been supported by the European Research Council, Starter Grant #337187 and Marie Curie Career Integration Grant (CIG) # 334303.

Conflict of Interest: none declared.

References

Annibale, P., *et al.* (2010) Photoactivatable Fluorescent Protein mEos2 Displays Repeated Photoactivation after a Long-Lived Dark State in the Red Photoconverted Form, *Journal of Physical Chemistry Letters*, **1**, 1506-1510.

Annibale, P., *et al.* (2011) Identification of clustering artifacts in photoactivated localization microscopy, *Nat. Meth.*, **8**, 527-528.

Annibale, P., *et al.* (2011) Quantitative Photo Activated Localization Microscopy: Unraveling the Effects of Photoblinking, *PLoS ONE*, **6**, e22678.

Babich, A., *et al.* (2012) F-actin polymerization and retrograde flow drive sustained PLCγ1 signaling during T cell activation, *The Journal of cell biology*, **197**, 775-787.

Bathe, M., *et al.* (2008) Cytoskeletal Bundle Mechanics, *Biophysical Journal*, **94**, 2955-2964.

Baumgart, F., *et al.* (2016) Varying label density allows artifact-free analysis of membrane-protein nanoclusters, *Nat. Meth.*, **13**, 661-664.

Beemiller, P. and Krummel, M.F. (2010) Mediation of T-Cell Activation by Actin Meshworks, *Cold Spring Harbor Perspectives in Biology*, **2**.

Betzig, E., *et al.* (2006) Imaging Intracellular Fluorescent Proteins at Nanometer Resolution, *Science*, **313**, 1642-1645.

Bromley, S.K., *et al.* (2001) The Immunological Synapse, *Annual Review of Immunology*, **19**, 375-396.

Burkhardt, J.K., Carrizosa, E. and Shaffer, M.H. (2008) The Actin Cytoskeleton in T Cell Activation, *Annual Review of Immunology*, **26**.

Claessens, M.M.A.E., *et al.* (2006) Actin-binding proteins sensitively mediate F-actin bundle stiffness, *Nat. Mater.*, **5**, 748-753.

Dempsey, G.T., *et al.* (2011) Evaluation of fluorophores for optimal performance in localization-based super-resolution imaging, *Nat. Meth.*, **8**, 1027-1036.

Gowrishankar, K., *et al.* (2012) Active Remodeling of Cortical Actin Regulates Spatiotemporal Organization of Cell Surface Molecules, *Cell*, **149**, 1353-1367.

Heilemann, M., *et al.* (2008) Subdiffraction-Resolution Fluorescence Imaging with Conventional Fluorescent Probes, *Angewandte Chemie International Edition*, **47**, 6172-6176.

Hess, S.T., Girirajan, T.P.K. and Mason, M.D. (2006) Ultra-High Resolution Imaging by Fluorescence Photoactivation Localization Microscopy, *Biophysical Journal*, **91**, 4258-4272.

Kiuchi, T., *et al.* (2015) Multitarget super-resolution microscopy with high-density labeling by exchangeable probes, *Nat. Meth.*, **12**, 743-746.

Kusumi, A., *et al.* (2005) Paradigm shift of the plasma membrane concept from the two-dimensional continuum fluid to the partitioned fluid: High-speed single-molecule tracking of membrane molecules, *Annual Review of Biophysics and Biomolecular Structure*, **34**, 351-378.

Murase, K., *et al.* (2004) Ultrafine membrane compartments for molecular diffusion as revealed by single molecule techniques, *Biophysical Journal*, **86**, 4075-4093.

Nieuwenhuizen, R.P.J., *et al.* (2015) Co-Orientation: Quantifying Simultaneous Co-Localization and Orientational Alignment of Filaments in Light Microscopy, *PLOS ONE*, **10**, e0131756.

Ovesný, M., *et al.* (2014) ThunderSTORM: a comprehensive ImageJ plug-in for PALM and STORM data analysis and super-resolution imaging, *Bioinformatics*, **30**, 2389-2390.

Owen, D.M., *et al.* (2010) PALM imaging and cluster analysis of protein heterogeneity at the cell surface, *Journal of Biophotonics*, **3**, 446-454.

Prior, I.A., *et al.* (2003) Direct visualization of Ras proteins in spatially distinct cell surface microdomains, *Journal of Cell Biology*, **160**, 165-170.

Ripley, B.D. (1977) Modelling spatial patterns, *Journal of the Royal Statistical Society B*, **39**, 172-192.

Rust, M.J., Bates, M. and Zhuang, X. (2006) Sub-diffraction-limit imaging by stochastic optical reconstruction microscopy (STORM), *Nat. Meth.*, **3**, 793-796.

Sage, D., *et al.* (2015) Quantitative evaluation of software packages for single-molecule localization microscopy, *Nat. Meth.*, **12**, 717-724.

Sengupta, P., *et al.* (2011) Probing protein heterogeneity in the plasma membrane using PALM and pair correlation analysis, *Nat. Meth.*, **8**, 969-975.

Thompson, R.E., Larson, D.R. and Webb, W.W. (2002) Precise Nanometer Localization Analysis for Individual Fluorescent Probes, *Biophysical Journal*, **82**, 2775–2783.

Valades Cruz, C.A., *et al.* (2016) Quantitative nanoscale imaging of orientational order in biological filaments by polarized superresolution microscopy, *Proceedings of the National Academy of Sciences*, **113**, E820-E828.

van de Linde, S., *et al.* (2010) The effect of photoswitching kinetics and labeling densities on super-resolution fluorescence imaging, *Journal of Biotechnology*, **149**, 260-266.

Williamson, D.J., *et al.* (2011) Pre-existing clusters of the adaptor Lat do not participate in early T cell signaling events, *Nat. Immunol.*, **12**, 655-662.